Fluorocarbon-driven pore size reduction in polyurethane foams: an effect of improved bubble entrainment

Martin Hamann, Guillaume Cotte-Carluer, Sébastien Andrieux, Daniel Telkemeyer, Meik Ranft, Markus Schütte, Wiebke Drenckhan-Andreatta

Fluorocarbon-driven pore size reduction in polyurethane foams: an effect of improved bubble entrainment

Martin Hamann[1], Guillaume Cotte-Carluer[1], Sébastien Andrieux[1], Daniel Telkemeyer[2], Meik Ranft[3] , Markus Schütte[2], Wiebke Drenckhan[1]

[1]CNRS-UPR 22, Institut Charles Sadron, Université de Strasbourg, 67200 Strasbourg, France
[2]BASF Polyurethanes GmbH, 49448 Lemförde, Germany
[3]BASF SE, 67056 Ludwigshafen am Rhein, Germany

Abstract

Polyurethane (PU) foams are created via the chemical reactions arising after the blending of two initially liquid components (polyols and isocyanates). They are widely used for thermal insulation, for which a small pore size is required. Some of the most efficient pore size-reducing agents have proven to be per- and polyfluorinated carbons (FCs) which are simply added in small quantities to the initial liquid mixture. However, despite their long-standing use, their modes of action have only recently begun to be studied in detail. One widely accepted explanation of their action is that they supposedly suppress diffusional gas exchange between bubbles in the liquid-foam-state of the nascent PU foam (foam coarsening). However, using a new double-syringe mixing technique, we show that FCs actually act at a much earlier state of the process: they facilitate the entrainment of tiny air bubbles into PU foam systems during the initial blending processing. These bubbles serve as sites for heterogeneous nucleation during the foaming process, and their large number leads to a significant reduction of the characteristic pore size. More importantly, we also demonstrate that the same overall relation is found between the air bubble density and the final pore size for systems with- and without FC. Combined with a detailed analysis of the pore size distribution, we argue that the main pore size reducing effect of FCs is to facilitate air entrainment and that foam aging-related effects only play a minor role.

Keywords: Polyurethane foam, fluorocarbon, bubble entrainment, morphology, pore size.

1. Introduction

Rising energy prices and strict regulations on CO_2 emissions recently fueled the interest in optimizing polyurethane rigid (PUR) foams for thermal insulation, since they render both heating and cooling energetically more efficient. Minimizing the thermal conductivity of PUR foams has therefore become an important issue in the PUR foam industry[1]. One key aspect governing optimal thermal conductivity of PUR foams is their porous morphology with the requirement for small, closed pores and a narrow pore size distribution[2–4]. Thus, a well-known approach of improving PUR foams for thermal insulation is to minimize the characteristic pore size[5–7].

In this context, highly fluorinated hydrocarbons, or short, fluorocarbons (FCs), were found to not only serve as physical blowing agents[8,9] but also as liquid pore size reducing agents[10–13], since their use gives rise to PUR foams with a considerably decreased pore size. However, FCs are environmentally critical substances due to their high global warming potential (*GWP*)[14,15] and their persistent chemical nature, which may lead to an unwanted accumulation in the atmosphere[16]. Thus, it is desirable to substitute FCs as liquid pore size reducing agents by less critical alternatives. To do so, however, the physico-chemical origins of the FC-driven pore size reduction need to be understood in detail at first. While several reports[6,11,12] addressed the impact of FCs on the morphology and the material properties of PUR foams in a rather phenomenological manner, the underlying mechanisms responsible for the pore size reduction remain poorly understood despite the longstanding use of FCs. This is most prominently demonstrated by the fact that different explanations on how FCs achieve the pore size reduction are given in the preceding literature. For instance, the probably most widely accepted explanation evokes the inhibition of diffusional bubble coarsening in the initial liquid foam state of a PUR foam[17] due to FCs, whereas other explanations associate a reduction of the gas/liquid interfacial tension[6,11] or the generation of auxiliary bubble nuclei during FC evaporation[18] with the observed pore size reduction.

Advancing to solve this puzzle, *Brondi* et al.[19] very recently started analyzing the FC-driven pore size reduction from a mechanistical point of view. They also argue that FCs retard diffusional coarsening of the expanding gas bubbles during PUR foam blowing and solidification, which therefore gives rise to foams with a smaller mean pore size. However, they further demonstrate that FCs noticeably facilitate the entrainment of micrometric air bubbles into the initially liquid PUR foam system during the homogenization and blending of the reactive components. The importance of these entrained air bubbles has frequently been

mentioned to have a decisive impact on the formation of the porous PUR foam morphology[20–23], yet no quantitative investigations had been performed. Employing a new double-syringe mixing process, we recently showed for FC-free formulations that there is indeed a strong inverse correlation between the air bubble density in the reactive PUR foam mixture and the final mean pore size[24]. The advantage of this double-syringe mixing approach over most other processing techniques is that it allows for a precise control over the air entrainment into PUR foam systems and a systematic decoupling between air entrainment and the blending of the reactive components. Moreover, the sealed nature of the system minimizes premature evaporation of volatile components. Furthermore, we used this approach to propose a simple model which predicts the mean inverse pore volume given that the air bubble density is known[24]. Goal of the study at hand is to exploit the advantages of the double-syringe mixing technique to systematically study the impact of FCs on air entrainment and PUR foam generation. The question we aim to answer with this study is whether PUR foams prepared with- and without FC obey the very same correlation between air bubble density and pore size in order to distinguish whether the promotion of air entrainment or the inhibition of coarsening is the main mechanism responsible for the FC-driven pore size reduction.

2. Materials and methods

2.1 Materials

For all PUR foams, tripropylene glycol (TPG; 97% supplied by *Sigma Aldrich*) was used as a low-molecular polyol compound in the A-component. Furthermore, the A-component contained the amine-based catalyst Jeffcat ZR-50 (supplied by *Huntsman*) and the silicone-based surfactant Tegostab B8491 (supplied by *Evonik Industries*). Deionized water was used as a chemical blowing agent, while cyclopentane (reagent grade 98%, supplied by *Sigma Aldrich*) and optionally the fluorocarbon perfluoro(4-methylpent-2-ene) (90%, supplied by *abcr chemicals*) were used as physical blowing agents. For all formulations, the B-component consisted of the isocyanate Lupranat M20S which was supplied by *BASF*. Lupranat M20S is an oligomeric form of methylene diphenyldiisocyanate with an NCO-content of ca. 31 wt.% and an average functionality of 3. All chemicals were used as received without prior purification.

2.2 Formulations

For all PUR foams, the isocyanate-index remained fixed at I_{NCO} = 120. Moreover, the amount of blowing agents (deionized water, cyclopentane, and optionally perfluoro(4-methylpent-2-ene)) was chosen such that the final foams density was ρ = (30 ± 2) g L^{-1}. Note that for this reason, the cyclopentane concentration had to be slightly adjusted whenever the FC was used, since cyclopentane and the FC have different molecular masses (M_{CP} = 70.1 g mol^{-1} vs. M_{FC} = 300.1 g mol^{-1}). The surfactant concentration was c_{surf} = 2.00 wt.% and the catalyst concentration was c_{cat} = 1.55 wt.% for all formulations. Note that both c_{surf} and c_{cat} correspond to concentrations typically used in industrial R&D facilities for the preparation of PUR foams with good stability and reasonable reaction kinetics. Table 1 provides a detailed overview of the PUR foam formulations used throughout this study. In total, the mass of the overall reactive PUR foam systems containing the A-component, the B-component and the blowing agents was ca. 56 g.

Table 1: *Overview of the formulations used for PUR foam preparation.*

Substance	**Weight percent* [wt.%]**	
A-component (Σ *m* = 18.0 g)		
Tripropylene glycol	93.95	
Surfactant (Tegostab B8491)	2.00	
Catalyst (Jeffcat ZR50)	1.55	
Water	2.50	
Physical Blowing Agent		
Cyclopentane (CP)	13.5	13.0
Perfluoro-4-methylpent-2-ene (FC)	0	2.0
B-component (*m* = 35.64 g)		
Iso M20S **(I_{NCO} = 120)**	198	

* with respect to 100 wt.% of the A-component.

2.3 Methods

2.3.1. Preparation of PUR cup foams

Step I: Entrainment of air bubbles into the A-component

First, all substances of the A-component as well as the physical blowing agents were weighed into one 60 mL plastic syringe and mixed by gently whipping the syringe by hand such that the liquid appeared homogeneous. Special care was taken not to entrain air bubbles during the homogenization. Pushing the syringe piston while holding the syringe vertically, all excess air was removed such that the syringe contained only the liquid A-component and the physical blowing agents (in total ca. 17 mL). Next, this syringe was connected to another 60 mL plastic syringe containing 17 mL of air via a narrow silicone tubing (internal diameter d_{int} = 3.2 mm; external diameter d_{ext} = 4.8 mm) and a three-way valve as is shown in Figure 1b. The connected syringes were fixed within a home-built double-syringe mixing device (Figure 1a) which drives a periodic motion of a two-armed crankshaft to push the pistons of the connected syringes in an alternating fashion. Thus, the content of both syringes was pushed repeatedly through the narrow tubing which lead to the formation of air bubbles via air entrainment into the polyol-based A-component. To alter the number of air bubbles formed during the air entrainment step (step I in Figure 1b), we varied the number of mixing cycles N_c between air and the A-component (N_c = 0 ; 1 ; 2 ; 5 ; 10 ; 30 ; 50) while keeping the average speed of the crankshaft arms constant at $\langle v \rangle$ = 9 cm s^{-1}. For each N_c, a sample of the premix was deposited in the center of a microscope carrier slide (70 mm x 26 mm) directly after the air entrainment step. This slide was equipped with spacers of 44 µm thickness and covered by a second microscope carrier slide such that a monolayer of air bubbles was observed in a volume of ca. 0.33 mm^3 via transmitted white light using a *Keyence VHX 2000* microscope. Automatic image analysis via *ImageJ* (*National Institutes of Health*) was used to measure the number and size of entrained air bubbles per unit volume of the premix, i.e. the bubble density n_{pre}, and the mean bubble radius $\langle r_b \rangle$. Detailed information concerning the microscopy analysis is provided in the Supporting Information (SI Section 1). For every number of air entrainment cycles N_c, the microscopic characterization of the premix was repeated at least three times and a fresh premix was prepared for every repetition. Note that the premixes characterized via transmitted light microscopy could not be used further for the actual preparation of PUR foams and vice versa since rapid

execution after the air entrainment step is required for both microscopy and PUR foam generation. However, we found the process highly reproducible, so that we consider the characterized premixes representative for those used for the final reactive blending.

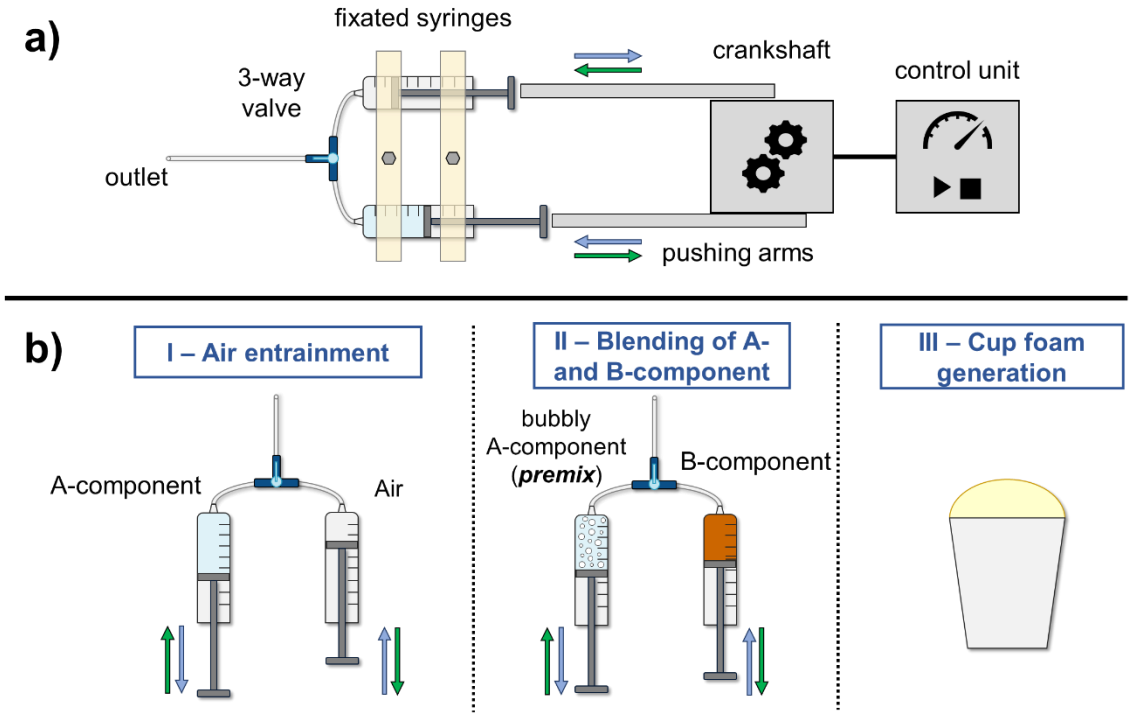

Figure 1: *a) Schematic drawing of the double-syringe mixing device used for the control of air entrainment during PUR cup foam preparation. b) Scheme of the applied procedure that allowed for both (I) controlled air entrainment and (II) the decoupling of entrainment and blending of the A- and B-component prior to PUR cup foam generation (III).*

Step II: Blending of the premix and the B-component

Directly after the end of the air entrainment step, the whole premix, i.e. the bubbly A-component, was collected in one of the two syringes and the empty syringe was replaced by a syringe pre-filled with the B-component. Note that the syringe containing the B-component was filled such that it did not contain any air. Then, the premix and the B-component were blended at room temperature using three blending cycles in the double-syringe machine at $\langle v \rangle$ = 9 cm s^{-1}. Due to the two syringes and their connections being sealed, no additional air was entrained into the system while the premix and the B-component were blended. As a consequence, the air bubble density of the premix n_{pre} is diluted by a factor f_{vol} = 0.38 upon blending of the premix and the B-component. Taking into account bubble aging in the period between the end of the premix generation and the end of the reactive blending step (decay to ca. 60 % of the initially

present bubble density within ~100 s as is shown in the Supporting Information Figure S5), the air bubble density *n* in the liquid reactive mixture can be calculated as

$$n = f_{\mathrm{vol}} \cdot f_{\mathrm{ag}} \cdot n_{\mathrm{pre}} = 0.38 \cdot 0.60 \cdot n_{\mathrm{pre}} \,. \qquad \textbf{[1]}$$

As we had shown in a preceding study[24], three blending cycles proved sufficient for properly blending the premix and the B-component while being short enough to avoid premature PUR foam blowing within the syringes.

Step III: PUR cup foam generation

After blending of the premix and the B-component was finished, the bubbly reactive mixture was ejected into a paper cup (V = 735 ml) at room temperature (20 °C) under a fume hood. Here, PUR foam blowing caused by both chemical blowing and physical blowing (the boiling point of both physical blowing agents being T_B = 49 °C) as well as solidification followed to eventually yield the final PUR foam. The cream time, i.e. the time where the onset of foam blowing could be observed, was (17 ± 3) seconds. We further defined the "gelling time" as the time at which thin polymer threads were pulled from the rising foam bun upon poking with a needle. This characteristic time occurred (64 ± 2) seconds after the mixing step. Both the value for the cream time and the gelling time correspond to mean values with standard deviations of at least three repetitions of the PUR foam preparation. Once foam formation was completed, the foams rested to cool down to room temperature. For each number of air entrainment cycles, three PUR foam samples were prepared for both the formulation with and without FC. There was no measurable different in the foam rise behavior of formulations with and without fluorocarbon.

Measurement of the PUR foam density

After the obtained PUR foam had cooled down to room temperature, the part of the foam that exceeded the height of the paper cup was cut off to align the foam volume and the cup volume (V = 735 mL). The density of the obtained PUR foam was obtained after removing the mass of the empty paper cup.

Characterization of the PUR foam morphology via scanning electron microscopy (SEM)

For SEM analysis, cubic samples with an edge length of ~5 cm were cut from the center of the PUR foam using a band saw as is shown in Figure 2. Then, thin slices of foam (thickness < 2 mm) were cut from each cubic foam sample using a razorblade (blue square indicated in Figure 2b). Two different slices were taken from opposing corners of the upper face of the cube that was orientated perpendicularly to the direction of foam rise. Additionally, a third slice was taken from the upper end of the foam bun. The foam slices were fixed on a SEM sample holder with an adhesive carbon tape that allows for dissipation of electric charges. A *Hitachi SU 8010* SEM was used for all SEM investigations. For image acquisition, secondary electron detection was used together with an accelerating voltage of 1.0 kV and a beam current of 10 µA.

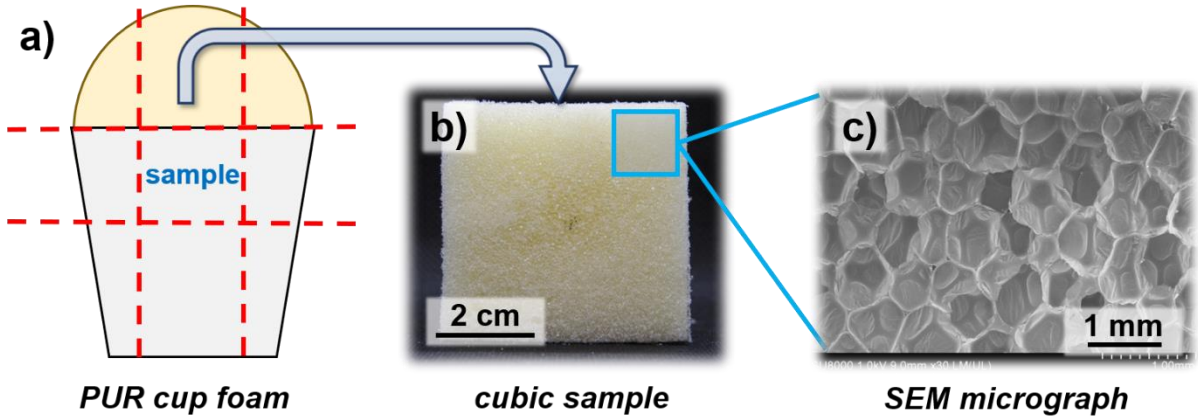

Figure 2: *a) Cuts through the cup foams (red dashed lines) for the preparation of cubic PUR foam samples b). Photograph of a cubic PUR foam sample obtained upon cutting of a cup foam. c) close-up image of the porous morphology of a cubic PUR foam sample acquired using scanning electron microscopy image (SEM).*

Determination of the mean pore size

The mean pore size was determined using the SEM micrographs. The micrographs were analyzed using ImageJ. First, pixel-scale was transferred to a micrometer-scale using the scale bar provided in the SEM micrographs. Then, brightness and contrast were adjusted such that the pore volume could be distinguished clearly from the pore edges. The "polygon selection" tool was used to manually construct polygons along the pores that describe the individual pores as good as possible. Then, the polygon areas A_{polygon}, i.e. the pore areas, were measured using the "measurement" tool. Eventually, the individual measured pore areas A_{polygon} were assigned to circular pores of the same area with a radius of

$$r_{\mathrm{c}} = \sqrt{\frac{A_{\mathrm{polygon}}}{\pi}}\,. \qquad \textbf{[2]}$$

Eventually, the arithmetic mean of the circular pore size r_{c}, i.e.,

$$\langle r_{\mathrm{c}} \rangle = \frac{1}{n}\sum_{i}^{n} r_{\mathrm{c},i}\,, \qquad \textbf{[3]}$$

was calculated. Lastly, a geometrical correction[25,26] was applied which accounts for the two-dimensional SEM analysis of three-dimensional foam pores was performed. Multiplying $\langle r_{\mathrm{c}} \rangle$ by correction factor of 1.273 considers the fact that most of the observed pores were not cut through their equator and that, in turn, the determined mean radii $\langle r_{\mathrm{c}} \rangle$ tend to be too small. Therefore, the corrected mean pore size $\langle r_{\mathrm{p}} \rangle$ used throughout this article is given by

$$\langle r_{\mathrm{p}} \rangle = 1.273 \cdot \langle r_{\mathrm{c}} \rangle\,. \qquad \textbf{[4]}$$

2.3.2. Surface tension measurements

Rising bubble tensiometry (*Tracker* tensiometer by *Teclis Scientific*) was used to study the interfacial tension between two distinct fluid phases via numerical assessment of the bubble shape. First, the liquid phases were prepared according to Table 2. After homogenizing the liquid phases using vigorous stirring via a magnetic stirrer (~1000 rpm for at least 30 seconds), the liquid phases were transferred to 25 mL quartz cuvettes. For all experiments, the liquid phase in the cuvettes was tempered at T = 20 °C for at least 30 minutes prior to starting the measurement to ensure constant thermal conditions. In case of FC-containing liquid phases, 500 µL of perfluoro(4-methylpent-2-ene) were added at the beginning of the tempering step and the liquid phase was gently stirred using a magnetic stirring bar throughout the experiment.

To minimize evaporation of the volatile FC, the cuvette was sealed with *Parafilm* as tightly as possible. The gas bubble volume was typically $V = 3 – 5$ µL. Note that air from the laboratory environment was used as gas phase. However, for experiments involving the FC in the liquid phase, the gas phase was saturated with FC-vapor by flushing the syringe that contained the gas phase 3 to 5 time with the supernatant vapor phase of a bottle containing liquid (volatile) perfluoro(4-methylpent-2-ene). All experiments were conducted statically, i.e. the volume of the rising bubble was maintained constant throughout the experiment via a PID-controller.

Table 2: *Overview of the formulations of the liquid- and gas phases used to study the impact of the FC on the surface tension of TPG-based premixes via rising bubble tensiometry.*

Liquid phase				
TPG [wt.%]	88	88	86	86
CP [wt.%]	12	12	12	12
Surfactant [wt.%]	-	-	2	2
FC [saturation]	-	✓	-	✓
Gas (vapor) phase				
Air	✓	✓	✓	✓
FC-vapor	-	✓	-	✓

3. Results and Discussion

3.1. Investigation of air entrainment during premixing

First, we investigated the impact of the FC on the entrainment of air bubbles into the TPG-based A-component using the double-syringe process with different numbers of entrainment cycles N_c (Section 2.3.1.). For both the formulation with- and without FC (Table 1), the microscopic premix characterization was repeated at least three times. Figure 3a and b show transmitted light micrographs of premixes prepared without and with FC directly after air entrainment for different numbers of N_c. Figure 3c plots the corresponding air bubble density , Figure 3d the mean bubble radius $\langle r_b \rangle$, and Figure 3e the mean gas volume fraction ϕ in the premix as a function of N_c.

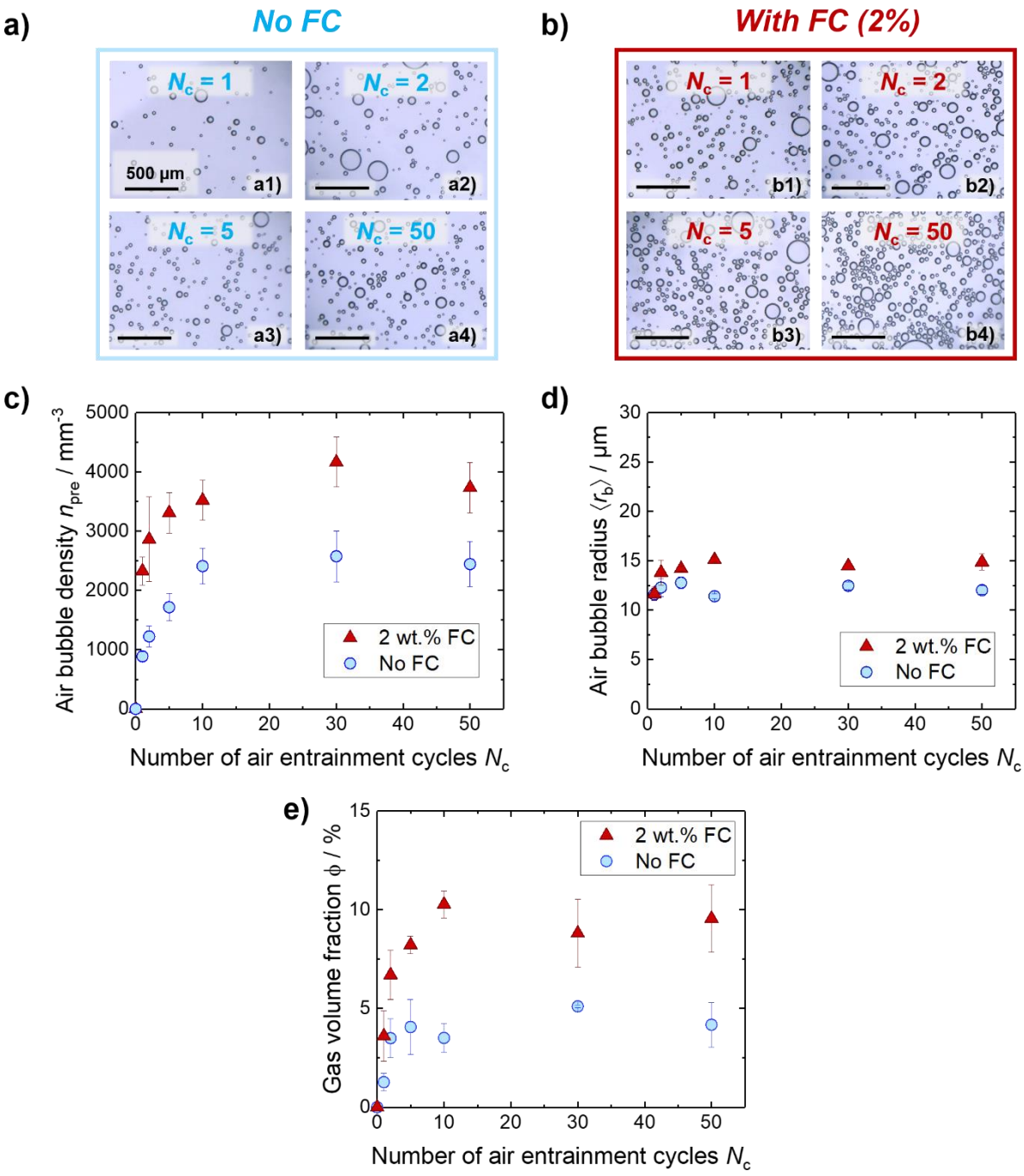

Figure 3: *Transmitted light microscopy images of bubbly A-components (premixes) a) without FC and b) with FC directly after the air entrainment step for increasing number of air entrainment cycles Nc. Diagrams of c) the air bubble density within the premix n_{pre}, d) the mean air bubble radius $\langle r_b \rangle$, and e) the gas volume fraction ϕ in the premix directly after air entrainment versus the number of air entrainment cycles N_c.*

Inspecting the micrographs shown in Figure 3a and b, together with the bubble density diagram shown in Figure 3c, two trends can be noticed. Firstly, many more air bubbles are observed in the presence of the FC. While the air bubble density in the premix n_{pre} ranges roughly between 900 and 2500 mm^{-3} for the FC-free A-component, bubble densities between 2300 and 4000

mm^{-3} are found in the presence of FC. Secondly, although the absolute bubble densities differ, the bubble density depends in a very similar manner on the number of mixing cycles N_c irrespective of the presence of the FC. This suggests that the FC does not fundamentally change the bubble formation mechanisms at play during air entrainment. For both formulations, a strong increase of the bubble density is found for low N_c, before a plateau is reached after ~10 air entrainment cycles. Next, Figure 3d shows that the mean bubble radius $\langle r_b \rangle$ remains fairly constant in the range of 10 - 15 µm independent of the number of air entrainment cycles N_c in both the absence and presence of FCs. Moreover, the addition of the FC does not fundamentally change the size of the entrained air bubbles even though the mean bubble radius $\langle r_b \rangle$ appears slightly increased in the presence of the FC.

The results presented in Figure 3c,d highlight the unique advantages of the double-syringe processing technique: For both A-components with- and without the FC, the air bubble density in the premix and, consequently, in the reactive PUR foam mixture, can be varied in a predictable manner via the number of air entrainment cycles without changing the characteristic bubble size. Therefore, the double-syringe technique is not only very well suited for studying how the addition of the FC affects the entrainment of air bubbles during (pre-)processing but also for correlating the pore size of PUR foams prepared with- and without FC to the initial air bubble density present in the liquid reactive mixture. Combining the information given in both Figure 3c and d, one finds that the gas volume fraction ϕ in the premix must be higher in case of the FC-containing premixes, since the mean bubble radius $\langle r_b \rangle$ remains nearly the same while the number of entrained bubbles is strongly increased. This is confirmed in Figure 3e, which plots the gas volume fraction in the premix directly after air entrainment over the number of air entrainment cycles N_c.

In this context, an important question is *why* the addition of the FC measurably increases the entrained gas volume fraction and with that the number of bubbles present in the premix. In fact, we made this observation[13] for different blending techniques (double-syringe blending, ultra turrax blending) and it has also been recently reported by Brondi et al.[19] for blending with a mechanical impeller. One mechanism may be that even though the same number of bubbles are generated with and without FC, the bubbles without FC undergo a more rapid ageing process. As is shown in Section 2 of the Supporting Information (Figures S4 and S5), the number of bubbles decreases rapidly over the first 100 s due to Ostwald ripening, which is driven by the high pressures in the small bubbles. Since about 100 s pass between the air entrainment step and the moment we start recording the bubbly mixture, a large number of

bubbles may have already disappeared. However, the two graphs in the SI show that, the FC has a negligible influence on the ripening process. This is in contrast to the argument that the FC acts as Ostwald ripening inhibitor in PUR foam formulations, which is often evoked in the literature and in patents[17,19]. This surprising lack of influence of the FC on the Ostwald ripening can be easily explained by the fact that the liquid and the gas matrix are both saturated with FC: even though the FC is not soluble in the A-component, it is present in the form of tiny droplets (as shown in the Supporting Information Figure S3) which diffuse and serve as efficient FC reservoirs. This saturation suppresses the osmotic pressure differences between bubbles which are required when FC is used as Oswald ripening inhibitor. We therefore think that the argument of the FC as Ostwald ripening inhibitor may be discarded.

An alternative argument may be that the FC has an influence on the air entrainment process itself, which is a complex hydrodynamic process arising in the extensional flow within the connector between the two syringes[27]. Since surface tension plays an important role in this process, we measured the surface tension of the bubbly premix without and with FC (Section 2.3.2.). Note that substances that were considered irrelevant for the measurement of the surface tension, i.e. the amine-based catalyst as well as the chemical blowing agent water, were not added to the A-component for the tensiometry experiments to minimize sources of contaminations and to highlight the impact of the FC on the surface tension. ***Figure 4*** shows the surface tension values obtained for simplified A-components containing only TPG, cyclopentane, and, optionally the silicone surfactant Tegostab B8941 both in absence and presence of the FC.

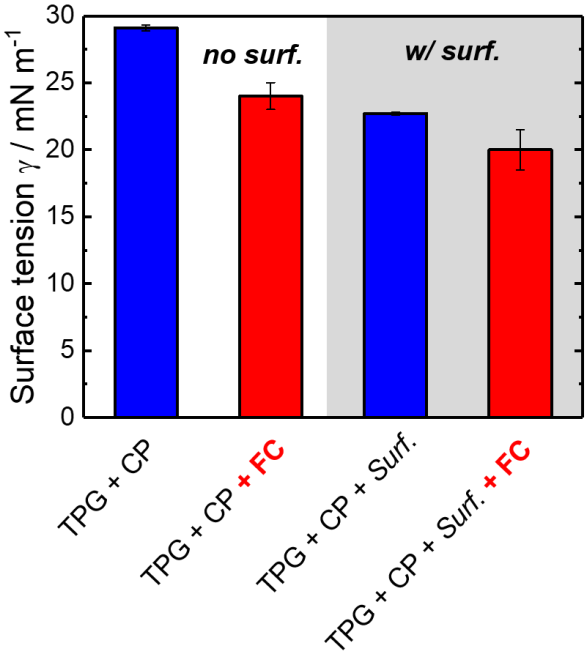

Figure 4: *Surface tensions of air bubbles in simplified A-components containing tripropylene glycol (TPG), cyclopentane (CP), and, optionally the silicone surfactant Tegostab B8941 (surf.) and/or the fluorocarbon perfluoro(4-methylpent-2-ene) (FC) using the formulations and measurement configurations given in Table 2.*

Figure 4 shows that the addition of the FC decreases the surface tension of the A-component by almost 20% from 29.1 mN m^{-1} to 24.0 mN m^{-1}. This seems surprising, since the utilized FC does not show a typical surfactant-like amphiphilic molecular structure and is therefore not expected to adsorb at the gas/liquid interface. What is even more surprising is the fact that even in the presence of the silicone surfactant, which is specifically designed to lower the surface tension by adsorbing at the gas/liquid interface, the surface tension is measurably lower in the presence of the FC (reduction by 2.7 mN m^{-1} which corresponds to roughly 10 %). This suggests that the FC co-adsorbs with the surfactant, altering the nature of the surfactant-laden bubble surface. In fact, the same behavior is known for similar fully-fluorinated hydrocarbons such as perfluorohexane[28,29]. For instance, it could be shown that, due to their very low surface energies, FCs adsorb at gas/liquid interfaces in aqueous systems altering the packing of other species present at the surface[29–33]. In this context, investigating in more detail if and how exactly the FC interacts with the silicone surfactant molecules at gas/liquid interfaces in PUR foam systems would definitely be an interesting study. However, addressing this topic was not within the scope of the study at hand.

Nonetheless, the results shown in Figure 4 still provide at least one potential explanation on why the addition of FCs favors the entrainment of more air bubbles. The reduction of the surface tension may facilitate air entrainment during premixing- and blending processes, which, in turn, leads to the generation of more gas bubbles during air entrainment. Although the underlying mechanisms behind the FC-driven reduction of the surface tension remain to be elucidated, this effect is reproducible and can be exploited.

3.2. Foam properties

Having characterized the bubbly premixes with- and without FC, we proceeded with blending them with the B-component using again the double-syringe mixing (Section 2.3.1, step II in Figure 1b). This allows to generate PUR foams from liquid reactive mixtures with well-controlled air bubble densities (step III in Figure 1b). Again, at least three PUR foams were prepared and characterized for each number of air entrainment cycles N_c. Figure 5a and b display photographs of a selection of PUR cup foams obtained for increasing N_c (i.e. with increasing air bubble density n in the reactive mixture) without and with FC respectively, as well as the corresponding SEM images.

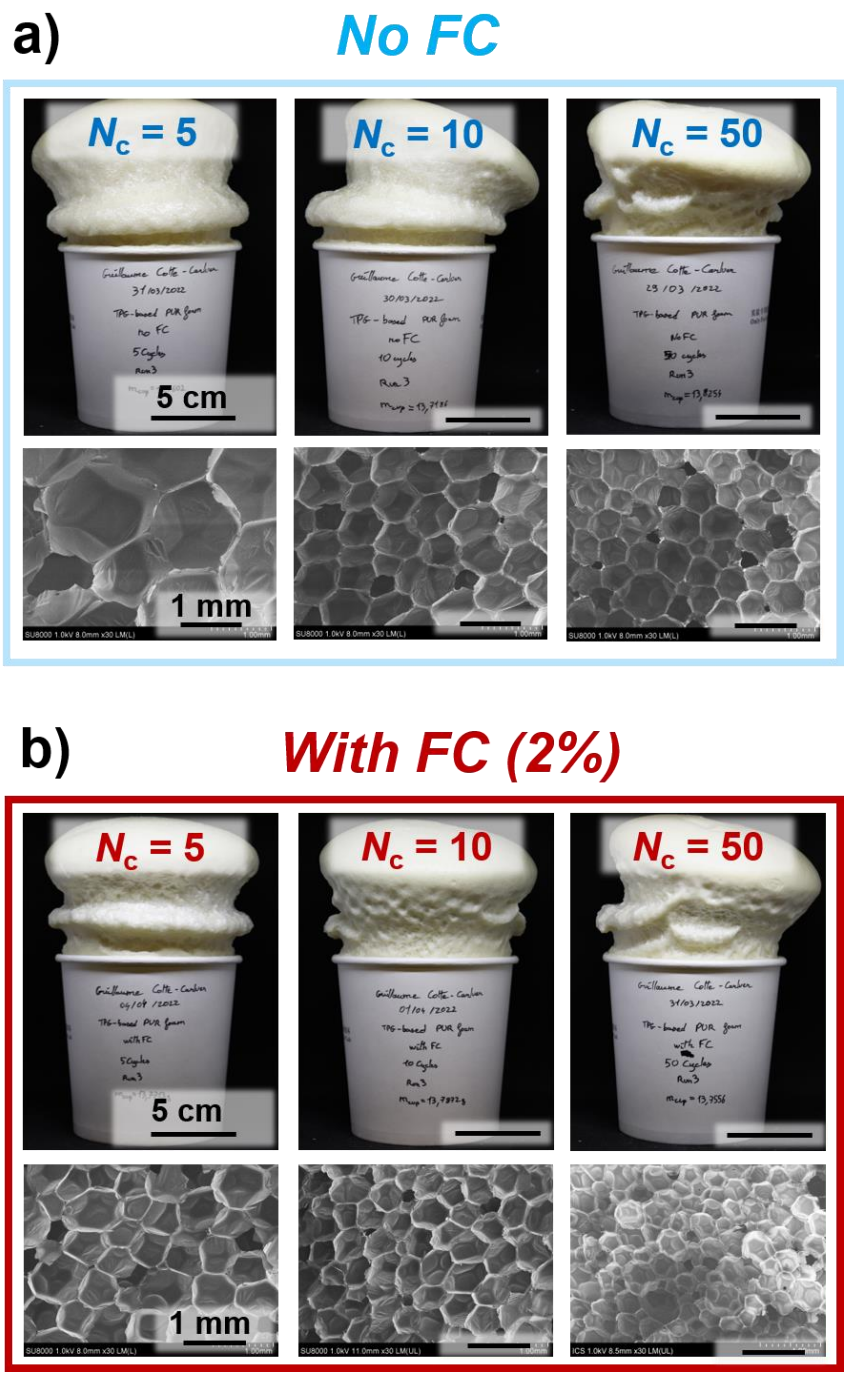

Figure 5: *Photographs and SEM images of PUR foams prepared with different number of air entrainment cycles N_c during premix generation. Samples prepared (a) without FC and (b) with FC.*

As can be seen in Figure 5a, the pore size of the PUR foams prepared without FC decreases with increasing number of air entrainment cycles N_c during pre-mix generation, which is in line with our previous study[24]. The same holds true for foams prepared with FC (Figure 5b). Comparing the foams prepared without and with FC, however, one finds that for any given number of air entrainment cycles, the FC-containing formulation gives rise to PUR foams with

considerably smaller pores. In our previous work[24] we demonstrated that there is a strong inverse correlation between the air bubble density *n* in the initially liquid PUR foam system and the final foam pore size $\langle r_p \rangle$. In Section 3.1. we showed that the addition of FC increases measurably the amount of air bubbles which are entrained during the double-syringe premixing. Hence, overall, it appears natural that these mixtures produce foams with smaller pores.

In order to investigate whether the same inverse correlation between the air bubble density and the pore size is found for PUR foams that were prepared with- or without the FC, we plot in Figure 5 the mean pore size $\langle r_p \rangle$ of the PU foams as a function of the air bubble densities *n* in the liquid reactive mixture. Here *n* is the air bubble density in the full liquid reactive mixture (premix + B-component), obtained from the bubble density n_{pre} in the premix (shown in Figure 5) via Equ. (1).

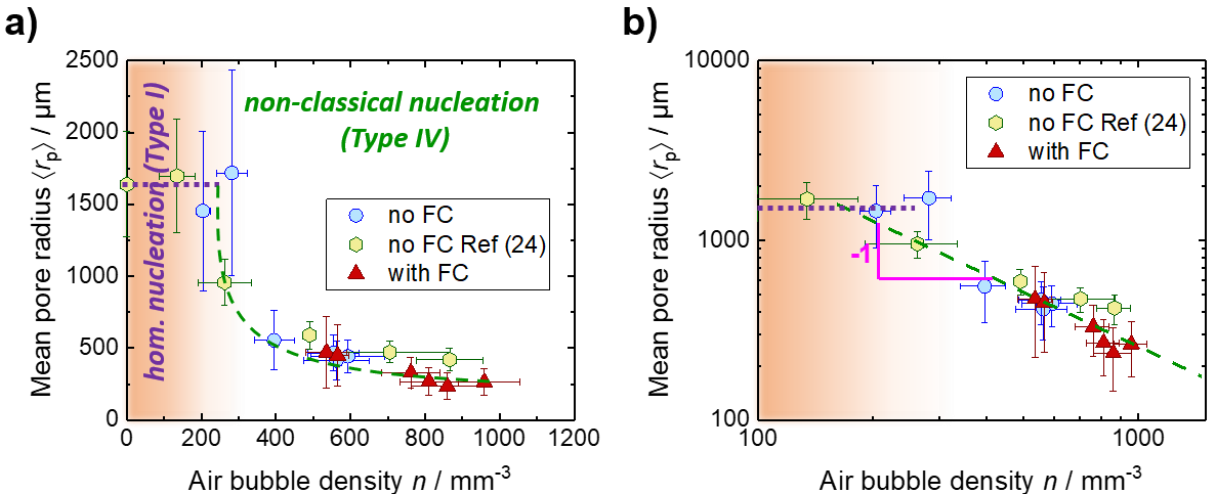

Figure 6: *Mean pore radius $\langle r_p \rangle$ of solid PUR foams versus initial air bubble density n in the corresponding liquid reactive mixture a) with linear axes and b) with logarithmic axes. The blue circles represent the PUR foams prepared without FC in the scope of the study at hand, while the yellow hexagons stand for the PUR foams prepared without FC in our previous study[24]. The red triangles represent the foams prepared with FC. The dashed area represents the regime of homogeneous bubble nucleation, whereas the clear area stands for the regime dominated by heterogeneous nucleation due the pre-dispersed air bubbles.*

Analysis of Figure 6a reveals several interesting results. Firstly, two different regimes seem to exist. For very low air bubble densities (colored zone), the mean foam pore size (~1600 µm) does not seem to depend on the bubble density. Surpassing an air bubble density of 200 – 300 mm^{-3}, however, the mean pore size decreases down to $\langle r_p \rangle$ = (250 ± 100) µm for the highest bubble densities in the range of 1000 bubbles per mm^3. This finding is remarkably well in line

with our previous study[24] on FC-free foams where the same trend was observed (yellow hexagons in Figure 6). As was previously discussed by *Brondi* et al.[34] and by us[24], this result can be explained as follows. In the absence of pre-dispersed air bubbles or for low bubble densities, bubble nucleation and therefore pore formation are driven by classical homogeneous nucleation (Type I) of liberated blowing agent vapor. In this case, the number of the nucleated gas bubbles as well as the transition of the bubbles to foam pores are determined by physico-chemical properties of the system such as reaction heat, surface tension, and gas supersaturation. However, increasing the air bubble density, non-classical type IV nucleation gradually becomes the dominating bubble/pore formation mechanism. Here, the number of pre-dispersed air bubbles is sufficient to absorb all the liberated blowing agent vapor such that no additional bubbles are nucleated upon liberation of the blowing agent vapor, since the energy barrier associated with the nucleation of new bubbles via classical nucleation is too high. In this case, increasing the number of air bubbles means that the blowing agent vapor volume released during PUR foam blowing is spread more evenly over the available air bubbles. As a consequence, the air bubble density and the mean pore size are inversely correlated in the air bubble-dominated regime.

However, the most remarkable result revealed by Figure 6a is that *all* mean pore sizes in the air bubble-dominated regime seem to follow *one and the same trend* with increasing bubble density – irrespective of the absence or presence of FCs! Having higher bubble densities, the FC-containing foams are simply pushed up to a higher range of the same trend. This result implies an important conclusion: The characteristic pore size of PUR foams is primarily controlled by the air bubbles entrained into the system during mixing and blending prior to the onset of any PUR foam-forming processes. Thus, we argue that the actual pore size-reducing mechanisms of the FC is to primarily increase the number of air bubbles that are formed during the (pre-)processing. Despite the fact that other mentioned pore size-reducing effects of FCs such as some slowing down of diffusional bubble coarsening or reduction of coalescence[29] are definitely plausible, we consider them as subordinate[13].

Plotting the data in Figure 6b using logarithmic axes, one notices that the observed correlation in the bubble dominated regime seems well described by a power law scaling $\langle r_p \rangle \sim n^{-1}$. In our previous work[24], we derived a simple scaling law $\langle r_p^3 \rangle \sim n^{-1}$ between the foam pore *volume* $\langle r_p^3 \rangle$ and the air bubble density n, using the assumption that all volatile components diffuse evenly into the pre-existing air bubbles. This leads to the simple relationship[24]

$$\langle r_p^3 \rangle = \frac{3}{4\pi} \frac{\varphi}{1-\varphi} \cdot n^{-1} \,, \qquad \textbf{[5]}$$

where φ is the porosity (gas fraction) of the final PUR foam. In Figure 7 we therefore replot the data using this scaling.

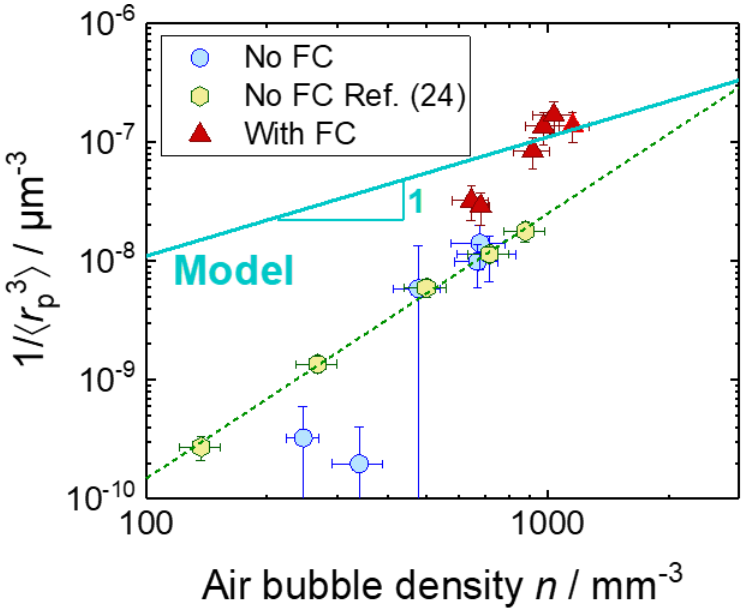

Figure 7: *Representation of the average pore volume obtained in the scope of this study using the notion of our previously proposed model*[24] *to describe the connection between the inverse pore volume* $1/\langle r_p^3 \rangle$ *and the air bubble density.*

As can be taken from Figure 7, the mean inverse foam pore volume of all PUR foams prepared *without* FC in the scope of this study as well as those prepared in our previous study[24], seem to follow roughly the same trend (green dashed line). Looking at the foams prepared *with* FC, however, the mean inverse foam pore volume $\langle r^3 \rangle^{-1}$ increases more steeply with increasing air bubble density n. This may indicate that there are in fact subtle differences for the foams prepared with or without FC despite the fact that Figure 6 suggests one global trend for *all* foams. This difference may show up more clearly when considering averages in the pore *volume* (rather than pore *radius*), which puts more emphasis on the large pores in the pore size distribution. However, in a previous work[13] - where we investigated the influence of the FC concentration on the pore size distribution - we could not identify a systematic shift in the pore size distribution. This question therefore requires more systematic investigation in the future.

Last but not least, Figure 7 shows that the assumption of an even distribution of all volatile components over the pre-existing air bubbles fails to capture reliably the data. It largely

underestimates the pre-factor of the correlation and fails to predict the experimentally observed inverse relationship $\langle r_p \rangle \sim n^{-1}$. Different effects may have yet to be taken into account to fully describe this correlation. First of all, one may need to consider more accurately the bubble density in the reactive mixture. While we have taken into account the aging of the bubbly pre-mix obtained from investigations of the bubbly A-component, the blending with the B-component may add additional ageing effects, including rapid dissolution of bubbles in the hydrophobic B-component. Moreover, the assumption of a homogenous distribution and absence of further foam ageing phenomena, as done in our model, is likely too simplistic, as shown by Brondi et al.[19] More quantitative investigations of this correlation for a wide range of formulations will therefore be required in the future, ideally using techniques which allow to follow the bubble and foam evolution continuously throughout the full process.

4. Summary and conclusion

The focus of the study at hand was to investigate how (per-)fluorinated carbons (FCs) influence the correlation between the number of entrained air bubbles in the premix and the final pore size of the PUR foam. Using a new double-syringe mixing process[24], we could show quantitatively that the presence of FC leads to a significant increase of the air bubble density which we claim to be the main reason why FCs act as pore size reducing agents. Thus, we once again exploited our double-syringe processing technique, which allows for a) controlling the air bubble density and b) for systematically decoupling air entrainment and the blending of the reactive PUR foam components, to correlate the air bubble densities in the initially liquid system to the final PUR foam pore size for formulations with- and without FC.

Our results clearly demonstrate that the addition of FCs to a PUR foam formulation favors the generation of higher air bubble densities during pre-mix generation via double-syringe mixing. To be more precise, air bubble densities ranged from 900 to 2500 bubbles per mm^3 for FC-free formulations, whereas bubble densities between 2300 and 4000 bubbles per mm^3 were found for formulations containing the FC. Moreover, the mean air bubble radius was consistently at ~15 µm and remained unaffected upon addition of the FC. One explanation for this increase in the air bubble density in presence of the FC may be found by looking at the surface tension, which decreases by roughly 20 % upon addition of the FC to the A-component. However, further studies are necessary to elucidate how exactly the FC alters the interfacial properties of the air bubbles and to monitor if other FC-driven physico-chemical effects not yet considered

also promote bubble entrainment. Quantitative in-situ investigations of the initial entrainment process will be required in the future, considering also the rheological properties of the formulations with and without FC and the high solubility of gases in the FC.

Next, we proceeded to mix the bubbly premixes with the isocyanate-based B-component using our double-syringe mixing device to generate PUR foams with well-controlled air bubble densities. In general, foams prepared in the presence of the FC had considerably smaller pores at any given number of air entrainment cycles: the mean pore size for FC-free foams ranged between 1600 µm and 400 µm while mean pore sizes between 500 and 250 µm were found for foams prepared with FC. Much more strikingly, however, our results highlight that the mean pore radii $\langle r_p \rangle$ of all the foams we prepared within the scope of this study and even those of a preceding study follow the same trend with increasing air bubble density n. In fact, we observe a power law scaling according to $\langle r_p \rangle \sim n^{-1}$ that captures surprisingly well how the mean pore radius $\langle r_p \rangle$ evolves with increasing air bubble density n irrespective of the formulation of the chosen foam and the considered study. This scaling is in disagreement with a model assuming that all volatile gases are homogeneously distributed over the existing gas bubbles[24].

Further experimentation and considerations are therefore required to properly explain the origins of the observed scaling. Nevertheless, the presented results imply a very important conclusion. The number of air bubbles entrained into PUR foam systems during processing is *the* main parameter determining the final pore size. While other effects on foam ageing are also plausible, we consider their impact on the final pore size to be secondary.

Acknowledgements

We are greatful to Leandro Jacomine, Jonathan Dijoux, Aurélie Hourlier-Fargette, Marie-Pierre Krafft, Dominique Langevin and Katja Steck for precious scientific discussions and technical help. The authors gratefully acknowledge the PLAMICS facility of the Institute Charles Sadron for providing access to the SEM.

Funding

This work has been financed by BASF and an ERC Consolidator Grant (agreement 819511 – METAFOAM). It also profited from an IdEx Unistra "Attractivity grant" (Chaire W. Drenckhan). Overall, it was conducted in the framework of the Interdisciplinary Institute

HiFunMat, as part of the ITI 2021-2028 program of the University of Strasbourg, CNRS and Inserm, was supported by IdEx Unistra (ANR-10-IDEX-0002) and SFRI (STRATUS project, ANR-20-SFRI-0012) under the framework of the French Investments for the Future Program.

ORCID ID

Martin Hamann https://orcid.org/0000-0001-8573-6217

Guillaume Cotte-Carluer https://orcid.org/0009-0008-8862-0541

Sébastien Andrieux https://orcid.org/0000-0002-9176-3294

Wiebke Drenckhan https://orcid.org/0000-0002-3879-4956

Supporting information

Supporting information for this article is available online.

References

(1) Eling, B.; Tomović, Ž.; Schädler, V. Current and Future Trends in Polyurethanes: An Industrial Perspective. *Macromol. Chem. Phys.* **2020**, *221* (14), 1–11. https://doi.org/10.1002/macp.202000114.

(2) Gibson, L. J.; Ashby, M. F. *Cellular Solids*; Cambridge University Press: Cambridge, 1997. https://doi.org/https://doi.org/10.1017/CBO9781139878326.

(3) Schuetz, M. A.; Glicksman, L. R. A Basic Study of Heat Transfer through Foam Insulation. *J. Cell. Plast.* **1984**, *20* (2), 114–121. https://doi.org/10.1177/0021955X8402000203.

(4) Glicksman, L.; Schuetz, M.; Sinofsky, M. Radiation Heat Transfer in Foam Insulation. *Int. J. Heat Mass Transf.* **1987**, *30* (1), 187–197. https://doi.org/10.1016/0017-9310(87)90071-8.

(5) Estravís, S.; Tirado-Mediavilla, J.; Santiago-Calvo, M.; Ruiz-Herrero, J. L.; Villafañe, F.; Rodríguez-Pérez, M. Á. Rigid Polyurethane Foams with Infused Nanoclays: Relationship between Cellular Structure and Thermal Conductivity. *Eur. Polym. J.* **2016**, *80*, 1–15. https://doi.org/10.1016/j.eurpolymj.2016.04.026.

(6) Kim, T. S.; Lee, Y.; Hwang, C. H.; Song, K. H.; Kim, W. N. Cryogenic Thermal Insulating and Mechanical Properties of Rigid Polyurethane Foams Blown with Hydrofluoroolefin: Effect of Perfluoroalkane. *J. Cell. Plast.* **2021**, *0* (0), 1–17. https://doi.org/10.1177/0021955X211062633.

(7) Kang, J. W.; Kim, J. M.; Kim, M. S.; Kim, Y. H.; Kim, W. N.; Jang, W.; Shin, D. S. Effects of Nucleating Agents on the Morphological, Mechanical and Thermal Insulating Properties of Rigid Polyurethane Foams. *Macromol. Res.* **2009**, *17* (11), 856–862. https://doi.org/10.1007/BF03218626.

(8) Londrigan, M. E.; Snider, S. C.; Trout, K. G. K-Factor Improvement via Perfluorinated Hydrocarbons. *J. Cell. Plast.* **1993**, *29* (6), 544–555. https://doi.org/10.1177/0021955X9302900603.

(9) Yu-Hallada, L. C.; McLellan, K. P.; Wierzbicki, R. J.; Reichel, C. J. Improved Rigid Insulating Polyurethane Foams Prepared with HCFCs and Perfluoroalkanes. *J. Cell. Plast.* **1993**, *29* (6), 589–596. https://doi.org/10.1177/0021955X9302900606.

(10) Volkert, O. PUR Foams Prepared with Emulsified Perfluoroalkanes as Blowing Agents. *J. Cell. Plast.* **1992**, *28* (5), 486–495. https://doi.org/10.1177/0021955X9202800503.

(11) Lee, Y.; Geun Jang, M.; Hyung Choi, K.; Han, C.; Nyon Kim, W. Liquid-Type Nucleating Agent for Improving Thermal Insulating Properties of Rigid Polyurethane Foams by HFC-365mfc as a Blowing Agent. *J. Appl. Polym. Sci.* **2016**, *133* (25). https://doi.org/10.1002/app.43557.

(12) Brondi, C.; Di Maio, E.; Bertucelli, L.; Parenti, V.; Mosciatti, T. The Effect of Organofluorine Additives on the Morphology, Thermal Conductivity and Mechanical Properties of Rigid Polyurethane and Polyisocyanurate Foams. *J. Cell. Plast.* **2021**, *58* (1), 121–137. https://doi.org/10.1177/0021955X20987152.

(13) Hamann, M.; Andrieux, S.; Schütte, M.; Telkemeyer, D.; Ranft, M.; Drenckhan, W. Quantitative Investigation of the Pore Size Reducing Effect of Perfluorocarbons in Polyurethane Foaming. *Colloid Polym. Sci.* **2023**, *301* (7), 763–773. https://doi.org/10.1007/s00396-023-05107-z.

(14) Hodnebrog; Etminan, M.; Fuglestvedt, J. S.; Marston, G.; Myhre, G.; Nielsen, C. J.; Shine, K. P.; Wallington, T. J. Global Warming Potentials and Radiative Efficiencies of Halocarbons and Related Compounds: A Comprehensive Review. *Rev. Geophys.* **2013**,

51 (2), 300–378. https://doi.org/10.1002/rog.20013.

(15) Jain, A. K.; Briegleb, B. P.; Minschwaner, K.; Wuebbles, D. J. Radiative Forcings and Global Warming Potentials of 39 Greenhouse Gases. *J. Geophys. Res. Atmos.* **2000**, *105* (D16), 20773–20790. https://doi.org/10.1029/2000JD900241.

(16) Mühle, J.; Ganesan, A. L.; Miller, B. R.; Salameh, P. K.; Harth, C. M.; Greally, B. R.; Rigby, M.; Porter, L. W.; Steele, L. P.; Trudinger, C. M.; Krummel, P. B.; O'Doherty, S.; Fraser, P. J.; Simmonds, P. G.; Prinn, R. G.; Weiss, R. F. Perfluorocarbons in the Global Atmosphere: Tetrafluoromethane, Hexafluoroethane, and Octafluoropropane. *Atmos. Chem. Phys.* **2010**, *10* (11), 5145–5164. https://doi.org/10.5194/acp-10-5145-2010.

(17) Klostermann, M.; Schiller, C.; Venzmer, J.; Eilbracht, C. Production of Fine Cell Foams Using a Cell Aging Inhibitor. US 2018/0327563 A1, 2018.

(18) Creazzo, J. A. Blowing Agents for Forming Foam Comprising Unsaturated Fluorocarbons. US 2007/0100010 A1, 2007.

(19) Brondi, C.; Mosciatti, T.; Di Maio, E. Ostwald Ripening Modulation by Organofluorine Additives in Rigid Polyurethane Foams. *Ind. Eng. Chem. Res.* **2022**, *61* (40), 14868–14880. https://doi.org/10.1021/acs.iecr.2c01829.

(20) Kanner, B.; Decker, T. G. Urethane Foam Formation— Role of the Silicone Surfactant. *J. Cell. Plast.* **1969**, *5* (1), 32–39. https://doi.org/10.1177/0021955X6900500104.

(21) Grünbauer, H. J. M.; Folmer, J. C. W. Polymer Morphology of CO2-blown Rigid Polyurethane Foams: Its Fractal Nature. *J. Appl. Polym. Sci.* **1994**, *54* (7), 935–949. https://doi.org/10.1002/app.1994.070540712.

(22) Reignier, J.; Alcouffe, P.; Méchin, F.; Fenouillot, F. The Morphology of Rigid Polyurethane Foam Matrix and Its Evolution with Time during Foaming – New Insight by Cryogenic Scanning Electron Microscopy. *J. Colloid Interface Sci.* **2019**, *552*, 153–165. https://doi.org/10.1016/j.jcis.2019.05.032.

(23) Merillas, B.; Villafañe, F.; Rodríguez-Pérez, M. Á. Nanoparticles Addition in Pu Foams: The Dramatic Effect of Trapped-Air on Nucleation. *Polymers (Basel).* **2021**, *13* (17), 1–11. https://doi.org/10.3390/polym13172952.

(24) Hamann, M.; Andrieux, S.; Schütte, M.; Telkemeyer, D.; Ranft, M.; Drenckhan, W.

Directing the Pore Size of Rigid Polyurethane Foam via Controlled Air Entrainment. *J. Cell. Plast.* **2023**, *0* (0), 1–14. https://doi.org/https://doi.org/10.1177/0021955X231152680.

(25) Kong, M.; Bhattacharya, R. N.; James, C.; Basu, A. A Statistical Approach to Estimate the 3D Size Distribution of Spheres from 2D Size Distributions. *GSA Bull.* **2005**, *117* (1–2), 244–249. https://doi.org/10.1130/B25000.1.

(26) Pinto, J.; Solórzano, E.; Rodriguez-Perez, M. A.; De Saja, J. A. Characterization of the Cellular Structure Based on User-Interactive Image Analysis Procedures. *J. Cell. Plast.* **2013**, *49* (6), 555–575. https://doi.org/10.1177/0021955X13503847.

(27) Gaillard, T.; Roché, M.; Honorez, C.; Jumeau, M.; Balan, A.; Jedrzejczyk, C.; Drenckhan, W. Controlled Foam Generation Using Cyclic Diphasic Flows through a Constriction. *Int. J. Multiph. Flow* **2017**, *96*, 173–187. https://doi.org/10.1016/j.ijmultiphaseflow.2017.02.009.

(28) Chernyshev, V. S.; Skliar, M. Surface Tension of Water in the Presence of Perfluorocarbon Vapors. *Soft Matter* **2014**, *10* (12), 1937–1943. https://doi.org/10.1039/c3sm52289j.

(29) Steck, K.; Hamann, M.; Andrieux, S.; Muller, P.; Kékicheff, P.; Stubenrauch, C.; Drenckhan, W. Fluorocarbon Vapors Slow Down Coalescence in Foams. *Adv. Mater. Interfaces* **2021**, 2100723. https://doi.org/10.1002/admi.202100723.

(30) Shi, D.; Liu, X.; Counil, C.; Krafft, M. P. Fluorocarbon Exposure Mode Markedly Affects Phospholipid Monolayer Behavior at the Gas/Liquid Interface: Impact on Size and Stability of Microbubbles. *Langmuir* **2019**, *35* (31), 10025–10033. https://doi.org/10.1021/acs.langmuir.8b03546.

(31) Gerber, F.; Krafft, M. P.; Vandamme, T. F.; Goldmann, M.; Fontaine, P. Fluidization of a Dipalmitoyl Phosphatidylcholine Monolayer by Fluorocarbon Gases: Potential Use in Lung Surfactant Therapy. *Biophys. J.* **2006**, *90* (9), 3184–3192. https://doi.org/10.1529/biophysj.105.077008.

(32) Ando, Y.; Tabata, H.; Sanchez, M.; Cagna, A.; Koyama, D.; Krafft, M. P. Microbubbles with a Self-Assembled Poloxamer Shell and a Fluorocarbon Inner Gas. *Langmuir* **2016**, *32* (47), 12461–12467. https://doi.org/10.1021/acs.langmuir.6b01883.

(33) Steck, K.; Dijoux, J.; Preisig, N.; Bouylout, V.; Stubenrauch, C.; Drenckhan, W. Fluorocarbon Vapors Slow down Coalescence in Foams: Influence of Surfactant Concentration. *Colloid Polym. Sci.* **2023**, *301* (7), 685–695. https://doi.org/10.1007/s00396-023-05129-7.

(34) Brondi, C.; Di Maio, E.; Bertucelli, L.; Parenti, V.; Mosciatti, T. Competing Bubble Formation Mechanisms in Rigid Polyurethane Foaming. *Polymer (Guildf).* **2021**, *228*, 123877. https://doi.org/10.1016/j.polymer.2021.123877.

Fluorocarbon-driven pore size reduction in polyurethane foams: an effect of improved bubble entrainment

Martin Hamann[1], Guillaume Cotte-Carluer[1], Sébastien Andrieux[1], Daniel Telkemeyer[2], Meik Ranft[3], Markus Schütte[2], Wiebke Drenckhan[1]

[1]CNRS-UPR 22, Institut Charles Sadron, Université de Strasbourg, 67200 Strasbourg, France
[2]BASF Polyurethanes GmbH, 49448 Lemförde, Germany
[3]BASF SE, 67056 Ludwigshafen am Rhein, Germany

Supporting Information

1. Characterization of bubbly A-components (premixes) via transmitted light microscopy

1.1. Experimental details

Directly after the bubble generation step, three or four drops of the fresh premix were collected in the center of a microscope slide (70 x 26 mm). Both ends of this microscope slide were equipped with one layer of adhesive tape (*Tesafilm Classic*, thickness = 44 µm). Then, the microscope slide was covered by a second microscope slide of the same size. Due to the presence of the adhesive tape layer on the bottom slide, a thin slit of 44 µm thickness filled with the fresh premix sample was formed in-between the two microscope slides (see Figure S1). This slit hindered superposition of multiple bubble layers which would otherwise complicate automatic image analysis.

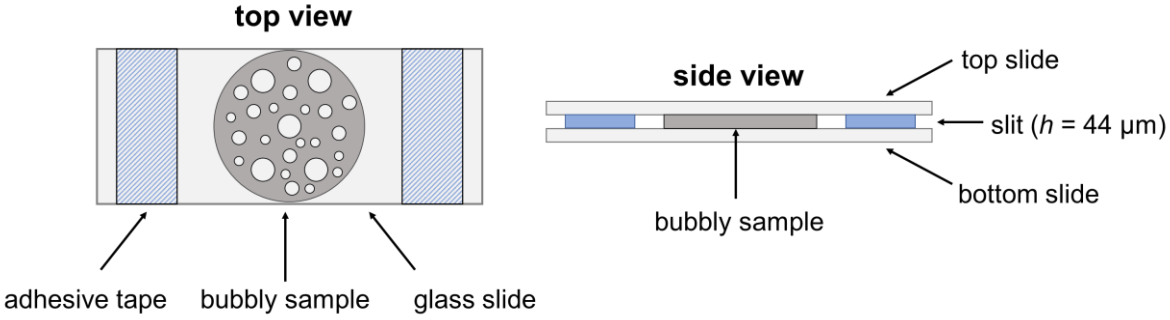

Figure S1: *Microscope slide setup used for the observation of bubbly polyol-based A-components (premix) in transmitted light mode*

All microscopic observations were conducted using a *Keyence VHX 2000* numerical microscope in transmitted light mode. To ensure fast and continuous image acquisition, videos of the samples were recorded for 600 s instead of single images, as the lowest rate of automatic single image acquisition was 5 seconds per image. All videos were recorded using a resolution of 1600 x 1200 pixels at a framerate of 15 fps. Using *VLC Player*, the recorded videos were then converted to single images such that one image for every second of the observation was generated.

Image analysis

All images were analyzed using the image analysis software *ImageJ* by *National Institute of Health*. For each image the same treatment was used to extract the number of bubbles and the mean radius. First, the images were binarized (8 bit). Next, the images were thresholded using Otsu's method. Then, the scale was set to translate pixel units into micrometer. Moreover, a window within the image in which bubbles were supposed to be considered was defined. Eventually, the "analyze particles" function of *ImageJ* was used for detecting the number of bubbles and the area of each bubble (see Figure S2).

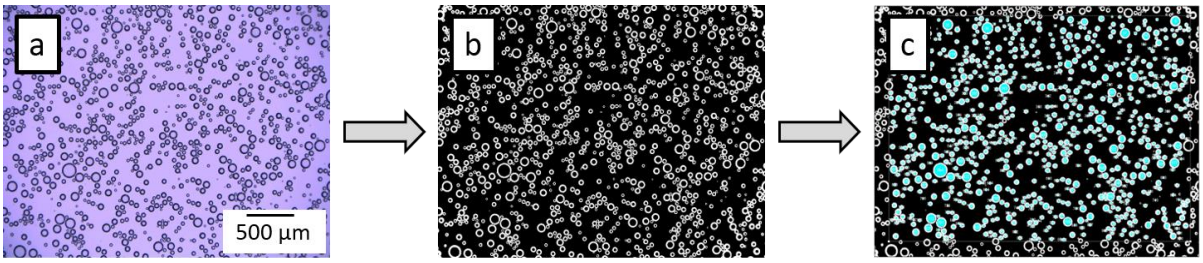

Figure S2: *Overview of the treatment of the microscope images: a) Raw image obtained from the microscope. b) Image after binarization and thresholding. c) Output of the particle analysis function of ImageJ.*

A macro that automated all the mentioned processing steps was generated and is supplied in the following:

```
run("8-bit");
folder="C:/Target_folder_path/" ;
Incomplete_name=getTitle();
name=Incomplete_name+".xls";
path=folder+name;
setAutoThreshold("Otsu dark");
```

```
//run("Threshold...");
//setThreshold(139, 255);
setOption("BlackBackground", false);
run("Convert to Mask");
//setTool("rectangle");
makeRectangle(68, 44, 1490, 1082);
run("Set Scale...", "distance=0.4653 known=1 pixel=1 unit=µm global");
run("Analyze Particles...", "size=30-Infinity circularity=0.60-1.00
show=[Overlay Masks] display exclude clear");
saveAs("Results", path);
```

Lastly, table calculations were used to convert the measured bubble areas into bubble radii. For air bubbles with a radius greater than half the slit thickness (r > 22 µm) the observed bubble radius had to be corrected since the observed air bubble was not spherical but had a "pancake shape" (which was approximated by a cylindrical shape) due to being confined between the two glass slides. The correction included calculating the volume of the observed cylindrical bubble and extracting the radius of a spherical bubble of equal volume.

$$r_s = \left(\frac{3}{4}h\right)^{\frac{1}{3}} \cdot r_c^{\frac{2}{3}} \quad \textbf{[1]}$$

With r_s being the diameter of a spherical bubble of equal volume to the observed cylindrical bubble, h the slit thickness (44 µm) and r_c the radius of the observed cylindrical bubble. Furthermore, the bubble count in the observed window was translated into a volumetric bubble density by dividing the bubble count by the volume of the observation window (V_{window} = 0.33 mm^3).

1.2. Microscopy of dispersed FC droplets

Having seen a pronounced turbidity when preparing FC-containing premixes and knowing that FCs are notoriously insoluble in most other liquid phases, we tried to use transmitted light microscopy to visualize the FC droplets and to assess their size. For this purpose, we zoomed into some of the premix samples that we used to study the temporal decay of the bubble density in the premix directly after its generation (see Section 2 of this supporting information). Figure S3 shows a micrograph of an FC-containing bubbly premix obtained using a magnification of 1000x.

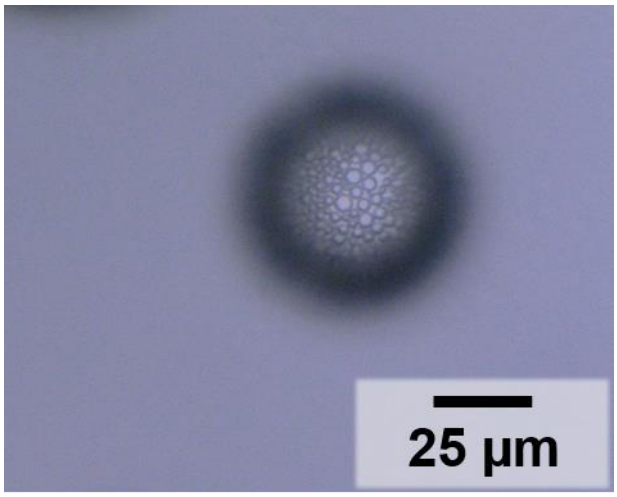

Figure S3: *High-magnification (1000x) transmitted light micrograph of an FC-containing bubbly premix.*

We observed that the FC droplets preferably accumulate at the bottom of the slit in between the two microscopic carrier slides shown in Figure S1. As can be taken from Figure S3, we found that the FC-droplets have a characteristic radius between 1 and 3 µm and are therefore very small with respect to the air bubbles ($\langle r_b \rangle$ = 10 – 15 µm). Although we managed to visualize the FC droplets, we emphasize that, due to their small characteristic size, other means of investigation such as light scattering techniques would be much more appropriate to characterize the FC droplets in more detail.

2. Microscopic analysis of bubble aging in the premix

To monitor the decay of the air bubble density n_{pre} in the premix due to bubble aging, transmitted light micrographs corresponding to t = [0, 5, 10, 15, 20, 25, 30, 40, 50, 100, 150, 200, 250, 300, 350, 400, 450, 500, 550, and 600] s were picked and evaluated for every experiments conducted using different cycle numbers N_c = [1, 2, 5, 10, 30, 50] both in absence and presence of the FC. In this context, Figure S4a and b show the evolution of the air bubble density as a function of time, while Figure S4c and d show the evolution of the corresponding mean bubble radii $\langle r_b \rangle$.

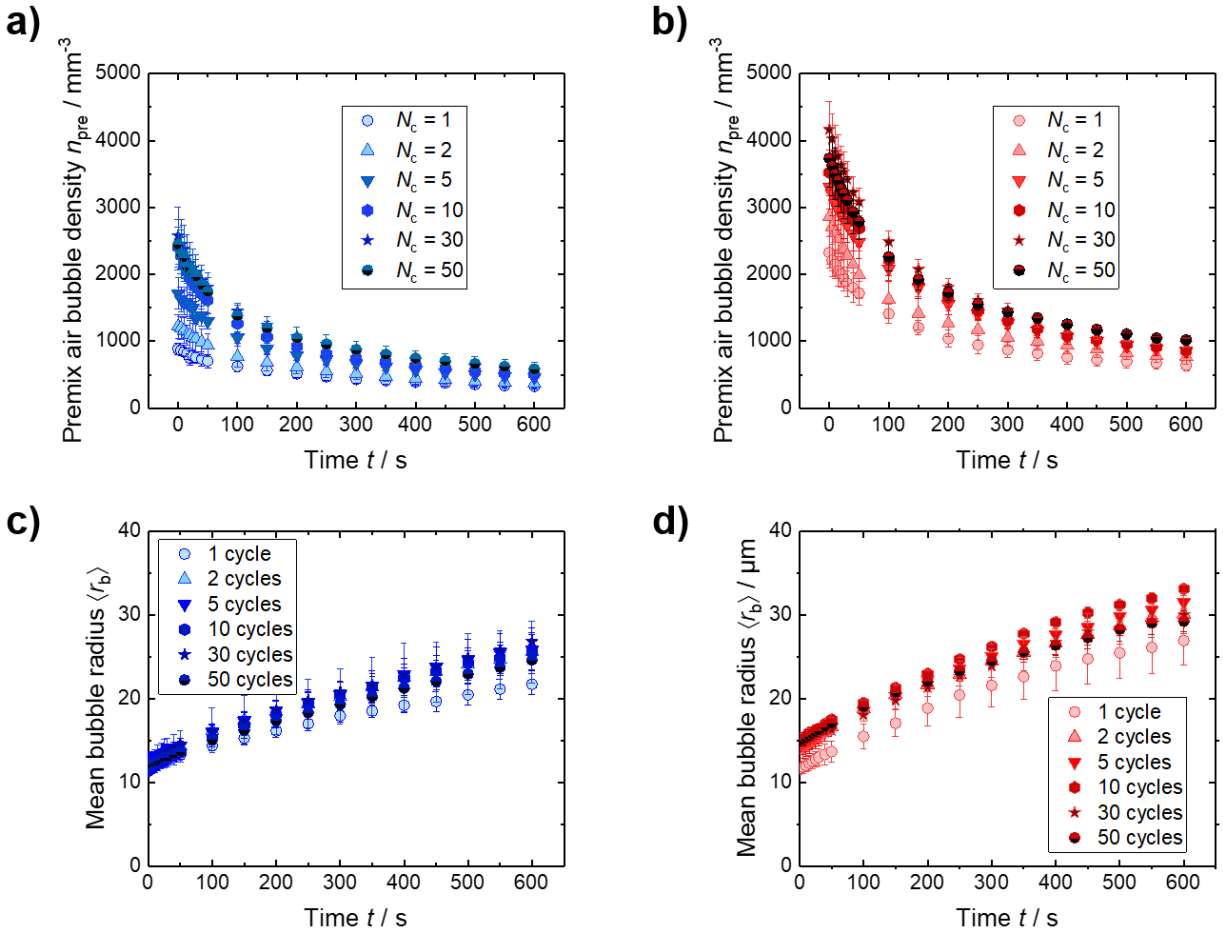

Figure S4:*Temporal evolution of the premix air bubble density n_{pre} for premixes generated a) without and b) with the fluorocarbon (FC) perfluoro(4-methylpent-2ene) using different numbers of mixing cycles N_c in a double-syringe mixing machine. Mean air bubble radius of the air bubbles in c) absence and d) presence of the FC in the premix.*

As can be taken from Figure S4a and b, the premix air bubble density n_{pre} decreases over the period of the microscopic observation with a pronounced decrease at the beginning of the observation irrespective of the absence or presence of the FC. At the same time, Figure S4c and

d show the mean air bubble radius $\langle r_b \rangle$ grows continuously during the observation for both formulations with and without FC. This demonstrates unambiguously that bubble aging is taking place in the premix and that the presence of the FC does not noticeably retard bubble aging as often stated.

For the sake of the comparability of the results shown in Figure S4, Figure S5a shows the temporal evolution of the normalized bubble density, i.e., how the bubble density n_{pre} changes with respect to the initial bubble density $n_{pre,0}$. Furthermore, the evolution of the normalized mean bubble radius $\langle r_b \rangle$ / $\langle r_{b,0} \rangle$ is shown in Figure S5. Note that for reasons of clarity, only the results of the experiments conducted with N_c = 50 are shown in Figure S5.

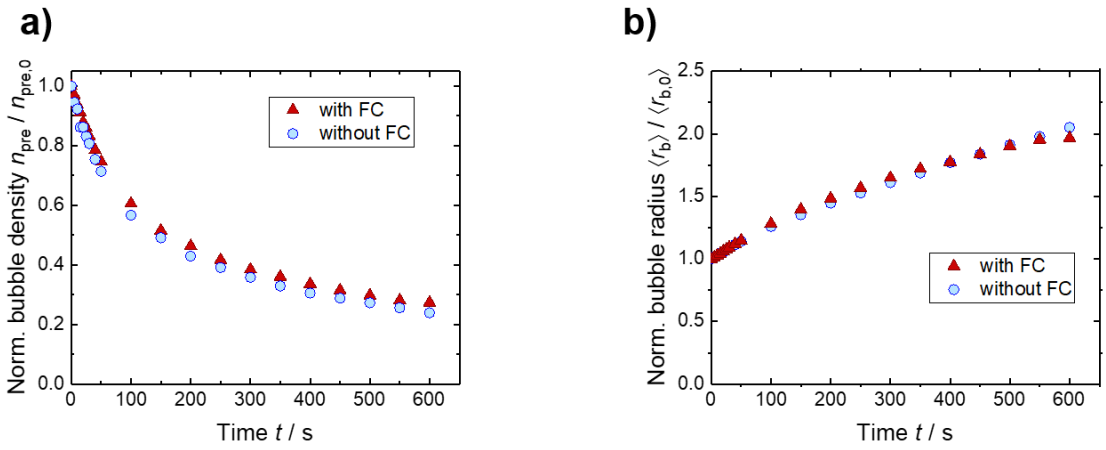

***Figure S5**:Temporal evolution of a) the normalized air bubble density n_{pre} / $n_{pre,0}$ and b) the normalized mean bubble radius $\langle r_b \rangle$ / $\langle r_{b,0} \rangle$ premixes generated using 50 double-syringe mixing cycles for formulations with and without the FC.*

Figure S5a reveals that the relative decay of the bubble density proceeds equally fast for formulations with and without the FC. As is shown in Figure S5, the same holds true for the growth of the entrapped air bubbles undergoing bubble aging. This finding emphasizes that bubble aging is not only not stopped in the presence of the FC – in fact it is not even noticeably decelerated.